Nanoscale

ROYAL SOCIETY OF CHEMISTRY

PAPER

View Article Online
View Journal | View Issue

Cite this: *Nanoscale*, 2023, **15**, 8654

Ultraflexible two-dimensional Janus heterostructure superlattice: a novel intrinsic wrinkled structure†

Kai Ren, *[a] Guoqiang Zhang,[b] Lifa Zhang,[c] Huasong Qin *[b] and Gang Zhang *[d]

Received 30th January 2023,
Accepted 15th April 2023

DOI: 10.1039/d3nr00429e

rsc.li/nanoscale

The recently reported two-dimensional Janus transition metal dichalcogenide materials present promising applications such as in transistors, photocatalysts, and thermoelectric nanodevices. In this work, using molecular dynamics simulations, the self-assembled in-plane MoSSe/WSSe heterostructure superlattice is predicted with a natural sinusoidal structure constructed by an asymmetric interface. Such a sinusoidal structure shows extraordinary mechanical behavior where the fracture strain can be enhanced up to 4.7 times than that of the symmetrical interface. Besides, the deformational structure of all these MoSSe/WSSe heterostructure superlattice are in accordance with the Fourier function curve; the fracture strength and fracture strain also demonstrate pronounced size dependence. Our investigations proposed an ultra-stretchable assembled heterostructure superlattice and provided a desirable strategy to tune the mechanical properties of such an in-plane two-dimensional heterostructure.

[a]*School of Mechanical and Electronic Engineering, Nanjing Forestry University, Nanjing, Jiangsu 210037, China. E-mail: kairen@njfu.edu.cn*
[b]*Laboratory for Multiscale Mechanics and Medical Science, SV LAB, School of Aerospace, Xi'an Jiaotong University, Xi'an 710049, China. E-mail: huasongqin@xjtu.edu.cn*
[c]*NNU-SULI Thermal Energy Research Center, and Center for Quantum Transport and Thermal Energy Science (CQTES), School of Physics and Technology, Nanjing Normal University, Nanjing 210023, China*
[d]*Institute of High Performance Computing, A*STAR, Singapore 138632, Singapore. E-mail: zhangg@ihpc.a-star.edu.sg*

†Electronic supplementary information (ESI) available. See DOI: https://doi.org/10.1039/d3nr00429e

Kai Ren

*Dr Kai Ren received his PhD in mechanical engineering from Southeast University in 2020. From 2019 to 2020, he also was a research assistant fellow at Prof. Zhang's group at the Institute of High Performance Computing, A*STAR, Singapore. He currently works as at Nanjing Forestry University and also is a post-doctoral candidate at Nanjing University of Aeronautics and Astronautics. His research is focused on the design of advanced functional material such as photocatalytic, photovoltaic, and optical devices.*

1. Introduction

Nowadays, two-dimensional (2D) materials are explored by abundant efforts, encouraged by graphene, which was found to possess extraordinary properties.[1] Although the Dirac cone in graphene contributes to ultrafast mobility,[2] such zero bandgap characteristic also restricts some applications such as field-effect transistors.[3] Thus, transition metal dichalcogenide (TMD) materials (MoS_2, WS_2, *etc.*) have attracted extensive research attention and also have high carrier mobility.[4] Besides, the decent bandgap of TMDs results in novel physical and chemical properties, such as photocatalyst for water splitting.[5,6] Recently, Janus MoSSe monolayer was prepared to reveal out-of-plane piezoelectricity for future spintronics[7] because of the broken symmetry. MoSSe and WSSe monolayers present thermal conductivity of about 51.27 W m^{-1} K^{-1} and 47.90 W m^{-1} K^{-1}, respectively, which still has obvious temperature dependence.[8] MoSSe was also found to be promising in various applications, such as photocatalyst,[9] electronics,[10] and energy conversion.[11,12] Besides, the novel magnetic and thermal performances are also explored for other 2D materials.[13–15]

For 2D materials, the effective strength of the monolayer used in engineering is decided by the fracture toughness instead of the intrinsic strength of atomic bonds. The failure characteristic of graphene results from a brittle manner, and the measured fracture toughness of graphene is about 4.0 MPa.[16] Negative Poisson's ratio is found in some 2D materials,

such as δ-SiSe (about −0.29),[17] Li_2B_{12} (about −0.03),[18] B_4N (about −0.02),[19] and δ-CS (about −0.19),[20] which is contributed by their particular structure. Such auxetic materials are promising candidates for composites and aviation.[21] Besides, 2D materials also illustrate desirable external strain-dependence on thermal[22] and electronic[23] performances. To create more applications for 2D materials, heterostructures are constructed. For example, van der Waals heterostructure possessing type-II band alignment can separate the photogenerated charges and prolong the lifetime of electrons and holes.[24] Differently, in-plane heterostructure is built by covalent bonding between the two materials. The in-plane MoS_2/WSe_2 heterostructure was recently synthesized,[25] and the fracture stress of the heterostructure can be tuned by interface, temperature, and introduced cracks.[26] The in-plane Janus MoSSe/WSSe heterostructure is also successfully prepared,[27] suggesting an intrinsic thermomechanical coupled interface.[28] Furthermore, the in-plane self-assembled heterostructure superlattice is obtained in experiments, such as WSe_2/WS_2,[29,30] which possesses diode characteristics with an ultrahigh rectification ratio of about 10^5. These heterostructure superlattices have excited critical consideration because of the novel quantum phenomena, such as mini-Dirac points,[31] Mott insulator states,[32] minimized lattice thermal conductivity,[33] and moiré exciton bands.[34] In particular, the band structure of the Janus MoSSe/WSSe superlattice can be changed from type-I to type-II by intrinsic structural parameters and used as a photocatalyst for water splitting,[35] which can also be effectively tuned by external strain and electric field.[36] The Janus MoSSe/WSSe superlattice nanoribbon can even be transformed as half-metal and magnetic material using decent ribbon width,[37] while the influence of superlattice configuration on the mechanical behaviors of the 2D in-plane heterostructure is rarely reported. In addition, the intrinsic bending at the interface of in-plane Janus MoSSe/WSSe heterostructure decides the mechanical strength, which can provide a theoretical guidance for further devices. However, the bending characteristic of the in-plane Janus MoSSe/WSSe heterostructure is not well investigated.

In this work, the in-plane Janus MoSSe/WSSe heterostructure superlattice is predicted to be stable with an almost sinusoidal structure by a decent interface. Then, the tunable mechanical behaviors of the heterostructure superlattice are investigated by different size parameters of the MoSSe and WSSe using molecular dynamics method, which shows an ultrastretchable characteristic.

2. Geometric structure and computational methods

In our investigation, all the simulations are implemented by Large-scale Atomic/Molecular Massively Parallel Simulator (LAMMPS).[38] The visualization of the atomic structure was obtained by the OVITO package.[39] The interatomic interactions of the in-plane MoSSe/WSSe heterostructure were employed by the Stillinger–Weber (SW) potential, which was proposed by Jiang and can provide the accurate prediction of the structure and mechanical properties of TMDs.[40,41] The stress–strain curve and the Young's modulus of MoS_2 calculated using this SW potential developed by Jiang is comparable with the experimental data,[42,43] which demonstrates the accuracy of the SW potential in studying the mechanical properties of this type of materials. The in-plane MoSSe/WSSe heterostructure superlattice was constructed referring in Fig. 1(a), where the total number of MoSSe and WSSe components is decided by N. Besides, the periodic boundary condition was set along the a, b, and c directions in the simulations. The length of the MoSSe, WSSe, and MoSSe/WSSe heterostructure was denoted as L_m, L_n, and L_0, respectively. Importantly, the possible interfacial types of the MoSSe/WSSe heterostructure were further demonstrated by Fig. 1(b)–(e), named as armchair-A (AA), armchair-B (AB), zigzag-A (ZA), and zigzag-B (ZB), respectively. For AA MoSSe/WSSe heterostructure in Fig. 1(b), the Se and S atoms are arranged on the same side in the MoSSe and WSSe with the armchair interface. To obtain the AB MoSSe/WSSe heterostructure, the Se and S atoms are located on the opposite sides in the MoSSe and WSSe. Similarly, the ZA and ZB MoSSe/WSSe heterostructure can be constructed. It is worth noting that the interfacial structure of the lateral MoSSe/WSSe can be synthesized in the experiment.[27,44–47] The size and periodicity of the TMDs heterostructure superlattice also can be controlled down to the nanometer scale.[30] Furthermore, to obtain a stable superlattice structure, the structure was relaxed by *NPT* ensemble (isothermal and isobaric) for 40 ns at 300 K with the time step of 1 fs. During the relaxation process, the temperature and energy of the system are monitored and reached a steady state. In addition, the layer thickness of the studied system was 0.61 nm.[41]

For the mechanical test, the uniaxial tension was conducted under a strain rate of 2×10^8 s^{-1} along the a direction using the fix/deform procedure in LAMMPS.[38] The temperature of the system was set as 300 K and zero pressure was applied along the b direction for the tensile deformation. To study the mechanical properties of the MoSSe/WSSe heterostructure superlattice, the normal stress was monitored in the calculations. The atomic virial stress of the Se, S, Mo, and W atoms is decided by

$$\sigma_i = \frac{1}{\Omega_i}\left[m_i v_i \otimes v_i + \frac{1}{2}\sum_{j\neq i} F_{ij} \otimes r_{ij}\right] \quad (1)$$

where Ω_i, m_i, and v_i represent the volume, mass, and velocity vectors of atom i, respectively. The force on atom I applied by atom j is F_{ij}. The distance between atom i and j is r_{ij}. In addition, the symmetric stress tensor (σ_i) is composed of σ_{xx}, σ_{yy}, σ_{zz}, σ_{xz}, σ_{xy}, and σ_{yz}, while σ_{xz}, σ_{yz}, and σ_{zz} can be ignored in the 2D system. Besides, the volume of each atom was obtained by the volume of the initial relaxed system divided by the total number of atoms.

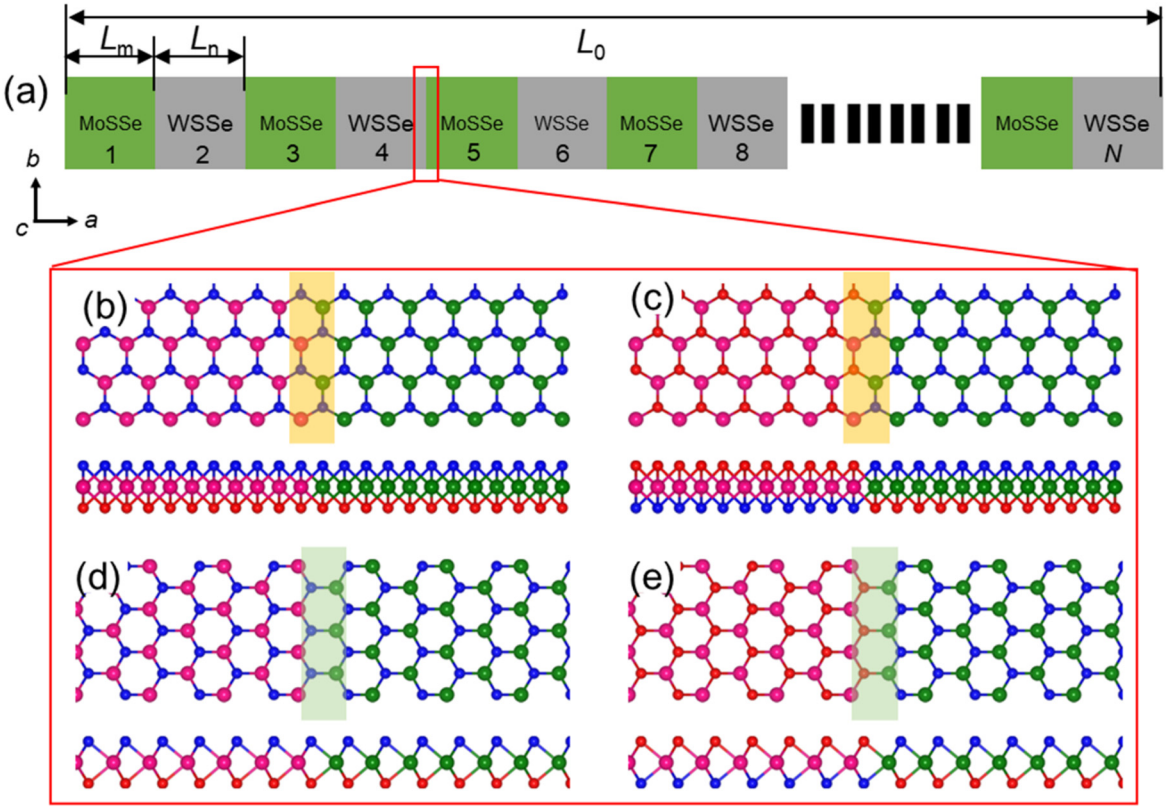

Fig. 1 (a) The diagrammatic sketch of the in-plane Janus MoSSe/WSSe heterostructure superlattice constructed with (b) AA, (c) AB, (d) ZA, and (e) ZB interface; the blue, pink, green, and red balls represent S, Mo, W, and Se atoms, respectively.

3. Results and discussion

The lattice constants of the MoSSe and WSSe monolayers are 3.228 Å and 3.269 Å, respectively, which have been reported in our previous work by first-principles calculations.[28] Thus, the lattice mismatch is about 1.26% for armchair and zigzag MoSSe/WSSe interface. Then, we design the self-assembled AA, AB (ZA and ZB) MoSSe/WSSe heterostructure superlattices. For the AA and AB MoSSe/WSSe heterostructure superlattices, the initial length and the width are 619.776 Å and 50.3195 Å, respectively. Besides, the initial length and width are 715.656 Å and 51.648 Å, respectively, for the ZA and ZB MoSSe/WSSe heterostructure superlattices. The periodic boundary condition is applied for the *a*, *b*, and *c* directions. In this work, the initial length and width of the total MoSSe/WSSe heterostructure superlattice are fixed, and the length of the MoSSe and WSSe sections is considered as a variable parameter.

Firstly, we explore the impact of the length ratio L_m/L_n on the optimized structure. After the structural relaxation, the intrinsic configurations of the AA and AB MoSSe/WSSe heterostructure superlattice with different L_m/L_n are presented in Fig. 2. Obviously, the AA heterostructure superlattice still presents an almost smooth monolayer, as shown in Fig. 2(a), (c), (e), (g), and (i), while the AB heterostructure superlattice folds regularly because of the interface bending, as shown in Fig. 2(b), (d), (f), (h), and (j). In particular, when L_m/L_n increases to 1, the nearly perfect sinusoidal structure monolayer is obtained, as shown in Fig. 2(j). This intrinsic characteristic is different from other analogous folding or wrinkled monolayers through external strain.[48–50] The same phenomenon also occurs in the heterostructure superlattice with a zigzag interface.

Inspired by the spontaneous bending structure of the MoSSe/WSSe heterostructure superlattice, the quantitative characteristics of such a trajectory were addressed. Here, to explore the tunable properties of the heterostructure superlattice, the length of the MoSSe and WSSe sections is fixed as $L = L_m = L_n$, as demonstrated in Fig. 1. Then, N is considered as 4, 8, 16, 32, and 64, which means that L should be 15.49 nm, 7.75 nm, 3.87 nm, 1.94 nm, and 0.97 nm, respectively, in AA and AB MoSSe/WSSe heterostructure superlattices. Similarly, L is 17.92 nm, 8.95 nm, 4.48 nm, 2.24 nm, and 1.12 nm in the calculations for the ZA and ZB MoSSe/WSSe heterostructure superlattices. We extracted the coordinate of the atoms in the *c* direction; after averaging them, the intermediate atomic coordinates are set as zero. Thus, the trajectories of the MoSSe/WSSe heterostructure superlattice is obtained. After the fitting method, we found that the side-view curves of all these relaxed structures follow Fourier function perfectly, the fitted Fourier function of the armchair and zigzag MoSSe/WSSe heterostructure superlattice with different L ($L = L_m = L_n$) is presented in Fig. 3(a). Clearly, the curve amplitude of these obtained

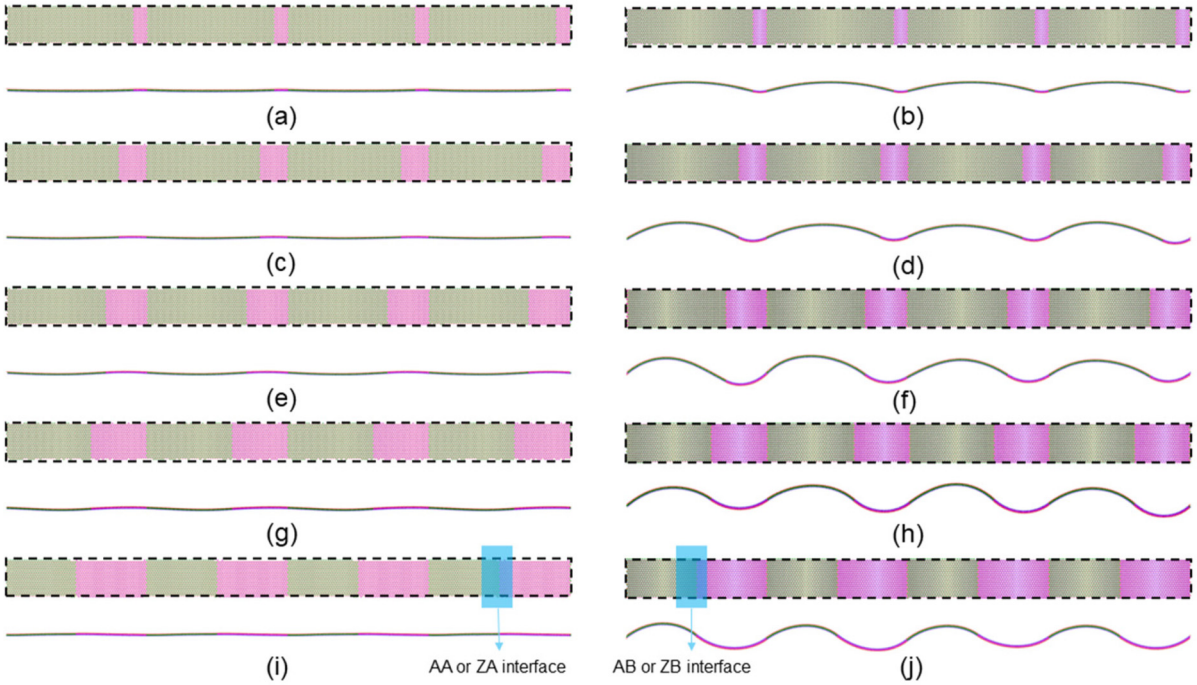

Fig. 2 The top and side views of optimized (a, c, e, g, and i) AA and (b, d, f, h, and j) AB Janus MoSSe/WSSe heterostructures with L_m/L_n as (a and b) 1/9, (c and d) 2/8, (e and f) 3/7, (g and h) 4/6, (i and j) 5/5, respectively.

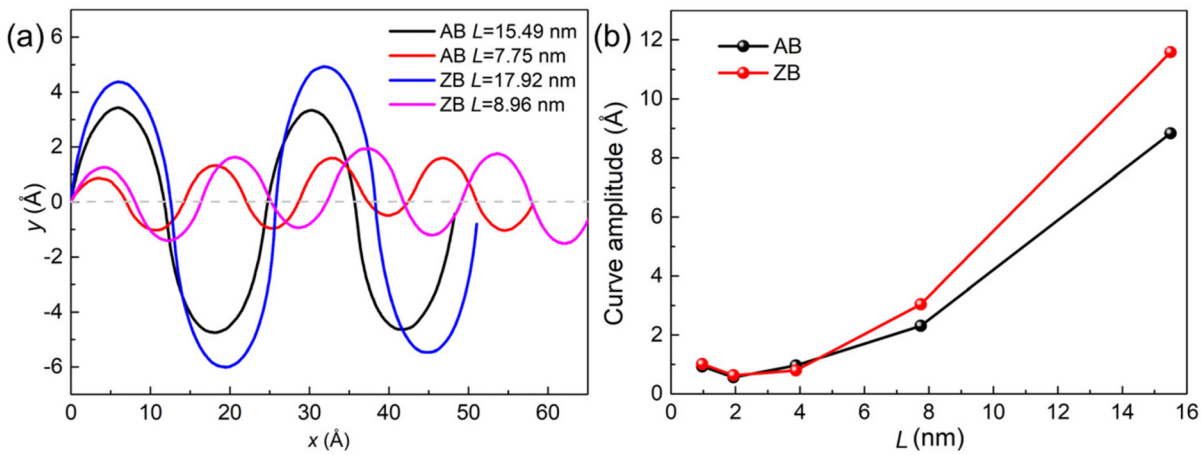

Fig. 3 (a) The fitted Fourier curve for the structural trajectory of the MoSSe/WSSe heterostructure superlattice and (b) the amplitude value of the Fourier curve *versus* *L*.

MoSSe/WSSe heterostructure superlattices can be enlarged by increased L, as shown in Fig. 3(b). This is because both sides of the individual MoSSe (or WSSe) section are applied to opposite intrinsic forces; when L_m (or L_n) is not long enough, the MoSSe (or WSSe) is hard to be bend. Thus, the curve amplitude decreases when L decreases. Furthermore, the functions of trajectories of the MoSSe/WSSe heterostructure superlattice in the Fig. 3(a) are also defined as $y = a\sin(bx) + c\cos(dx) + e$, which were fitted, and the details are presented in Table 1.

The fracture behaviors of the MoSSe and WSSe monolayers are calculated. For uniaxial tension along the armchair direction, the fracture strain of the MoSSe (or WSSe) monolayer is 0.113 (or 0.140) with the fracture stress of 12.66 GPa (or 19.85 GPa). While for uniaxial tension along the zigzag direction, the fracture strain of the MoSSe (and WSSe) monolayers is 0.100

Table 1 The obtained parameters for the functions of trajectories of the MoSSe/WSSe heterostructure superlattice

	a	*b*	*c*	*d*	*e*
AB L = 15.49	0.67	0.26	−4.36	0.26	0.071
AB L = 7.75	0.84	0.43	−0.79	0.43	0.050
ZB L = 17.92	−4.22	0.24	−3.97	0.24	−0.01
ZB L = 8.96	0.78	0.38	−1.31	0.38	−0.01

(and 0.120) with the fracture stress of 11.25 GPa (and 17.06 GPa), respectively. Obviously, the WSSe monolayer has higher mechanical strength than the MoSSe monolayer. Thus, the initial crack emerges in the MoSSe section in the MoSSe/WSSe heterostructure superlattice, as shown in Fig. 4, when the heterostructure superlattice is applied to the external strain. The crack nucleation of the MoSSe/WSSe heterostructure superlattice with AA, AB, ZA, and ZB interfaces are demonstrated by Fig. 4(a)–(d), respectively. Note that the atomic stress under tension along the zigzag MoSSe/WSSe heterostructure superlattice is larger, and the initial crack length is also longer. Furthermore, compared with the AA (or ZA) MoSSe/WSSe heterostructure superlattice, the required fracture stress is enhanced in AB (or ZB) heterostructure superlattice.

To further investigate the tunable strain–stress relationships of the MoSSe/WSSe heterostructure superlattice, the response of the stress on external uniaxial strain of the armchair and zigzag heterostructure superlattice is studied. The nonlinear elastic behavior is shown in Fig. 5. It is worth noting that the fracture strength of the AA (or ZA) and the AB (or ZB) MoSSe/WSSe heterostructure superlattice is comparable when L is 0.97 nm (or 1.12 nm). On the other side, the process of tension fracture for the AB and ZB MoSSe/WSSe heterostructure superlattice is prolonged substantially, as shown in Fig. 5(a) and (b); even the stress of the AB and ZB MoSSe/WSSe heterostructure superlattice remains very low before the strain increases to 0.28 and 0.38, respectively. This is because the relaxed state of the AB and ZB MoSSe/WSSe heterostructure superlattice is the bending structure; then, it needs to go through the process of being flattened before catastrophic damage, as shown in Fig. 5(c). Besides, the fracture stress MoSSe/WSSe heterostructure superlattice is higher than that of the MoS_2/WS_2 heterostructure (11.95 GPa along the zigzag direction and 12.55 GPa along the armchair direction) with N = 4.[26] Furthermore, the fracture strain with N = 4 is also much higher than that of the MoS_2/WS_2 heterostructure (9.6% along the zigzag direction and 9.4% along the armchair direction). Moreover, the stress–strain relationship of the AA MoSSe/WSSe heterostructure superlattice with L = 0.97 nm is also calculated by density functional theory (DFT) calculations. As shown in Fig. S1 in the ESI,† the results calculated using empirical potential agree well with those calculated using DFT, further demonstrating the accuracy of the SW potential used in this work.

The fracture stress of the MoSSe/WSSe heterostructure superlattice with armchair and zigzag interfaces with different L (here, we set $L = L_m = L_n$) are presented in Fig. 6(a). It can be seen that the MoSSe/WSSe heterostructure superlattice with zigzag interfaces possesses stronger fracture stress than that of armchair one, and all these heterostructure superlattices present a decreased fracture stress with L increasing. Importantly, the fracture stress of the AA (or ZA) MoSSe/WSSe

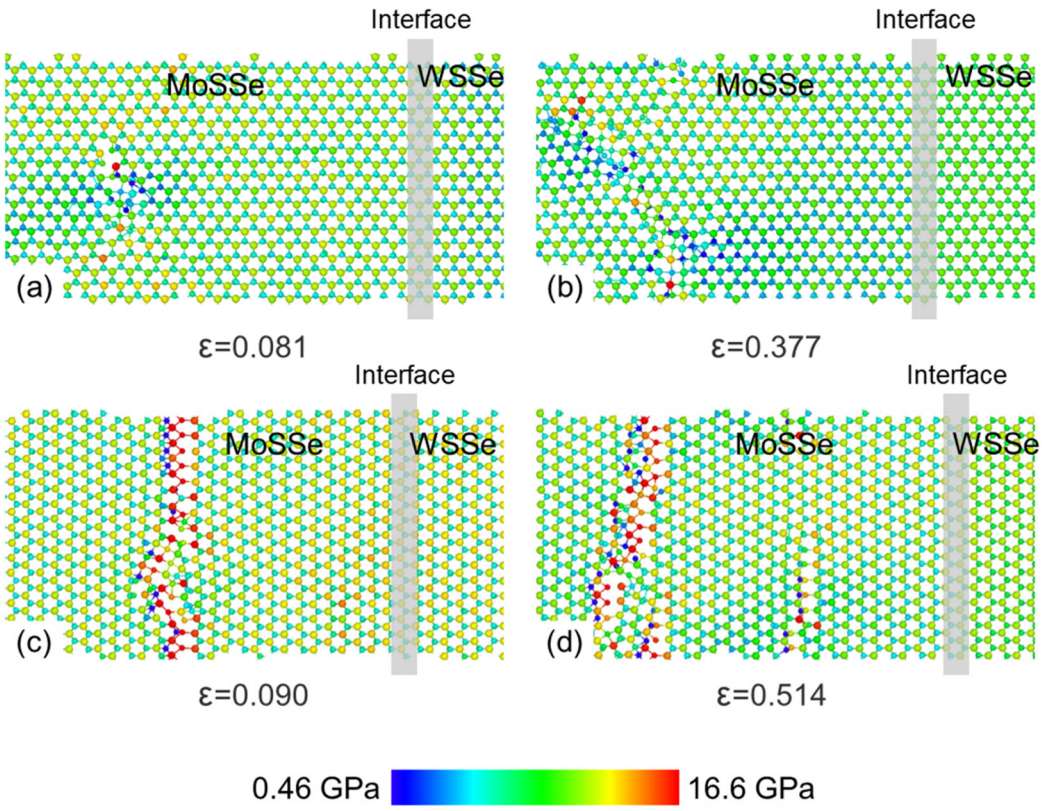

Fig. 4 The crack nucleation of the MoSSe/WSSe heterostructure superlattice with (a and c) AA and (b and d) AB interfaces. L is 15.494 nm and 17.92 nm, respectively, in (a and b) and (b and d).

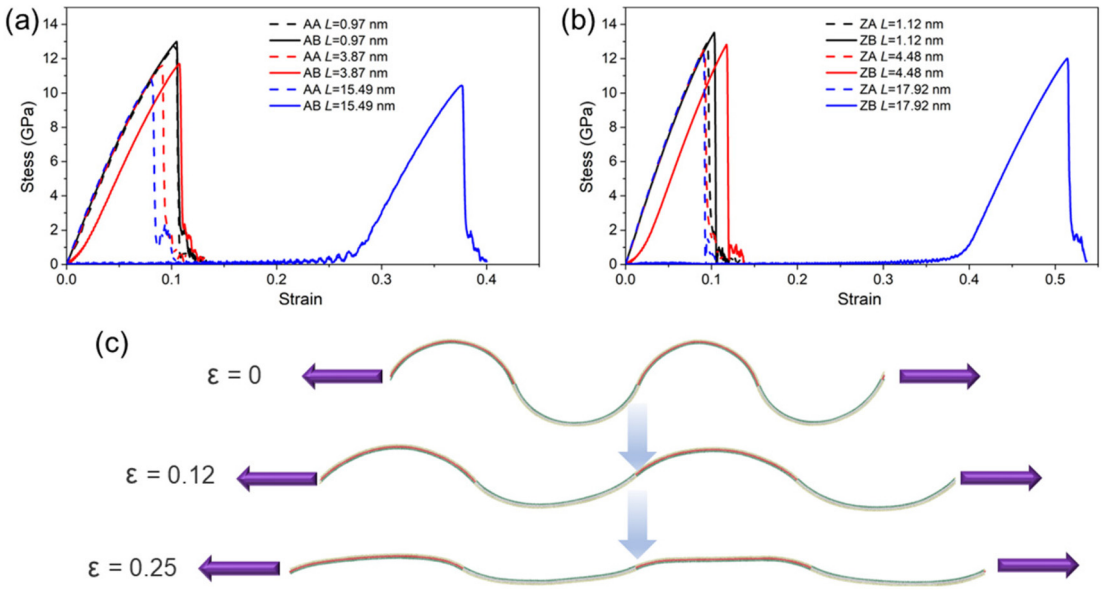

Fig. 5 The calculated stress–strain curves of the MoSSe/WSSe heterostructure superlattice with (a) armchair and (b) zigzag interfaces with different lengths L; (c) the side view of the structural evolution schematic for the AB MoSSe/WSSe heterostructure under uniaxial tension.

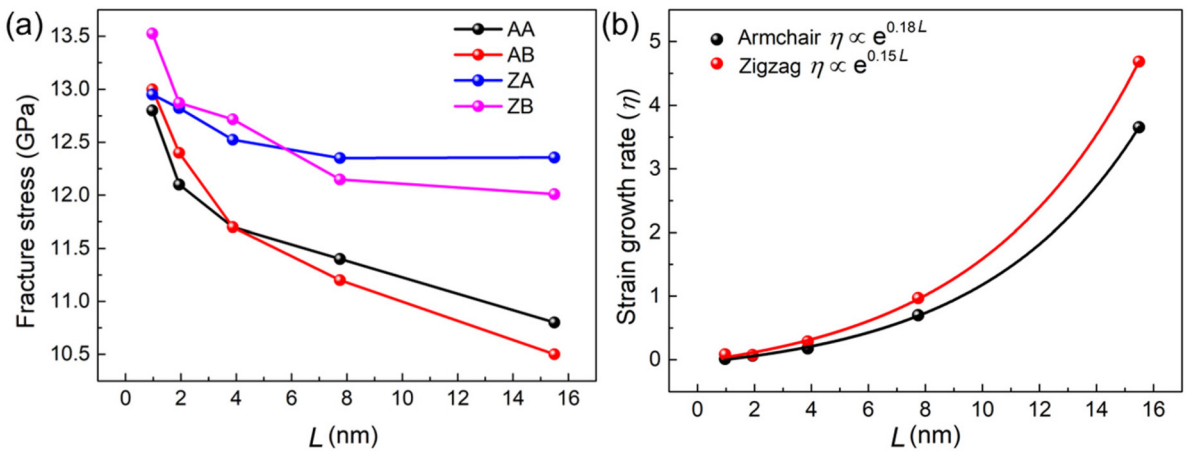

Fig. 6 (a) The obtained fracture of the MoSSe/WSSe heterostructure superlattice *versus* L; (b) the strain growth rate between the AA (or ZA) and AB (or ZB) at different L.

heterostructure superlattice can exceed that of the AB (or ZB) with increased L. Besides, the size-dependent fracture strain (σ_F) of the MoSSe/WSSe heterostructure superlattice is also studied. We use the fracture strain growth ratio (η), which is defined as $\eta = (\sigma_{F\text{-AB (or ZB)}} - \sigma_{F\text{-AA (or ZA)}})/\sigma_{F\text{-AA (or ZA)}}$, to evaluate the response of the fracture strain on L. As shown in Fig. 6(b), the rapid growth of η is obtained when L increases. In detail, the fracture strain of the AA (or ZA) MoSSe/WSSe heterostructure superlattices can be greatly improved by 3.7 (or 4.7) times using the AB (or ZB) interface. Therefore, the toughness of the MoSSe/WSSe heterostructure superlattice can be significantly enhanced by the asymmetric (AB and ZB) interface, which also illustrates the ultraflexible behavior. Furthermore, the exponential function relationship is found between the fracture strain growth and L, as shown in Fig. 6(b).

4. Conclusion

In this work, molecular dynamics calculations were performed to propose a new in-plane assembled heterostructure superlattice based on Janus MoSSe and WSSe. Four different interfaces are considered to construct the heterostructure superlattice and present thermal stability at 300 K. Interestingly, the AB and ZB MoSSe/WSSe heterostructure superlattice demonstrate excellent mechanical properties compared with that of the AA

and ZA interfaces as they need to overcome the intrinsic curved structure. The calculated fracture strain and the strength of the AB (or ZB) MoSSe/WSSe heterostructure superlattice are 0.38 (or 0.51) and 10.5 GPa (or 12.0 GPa) with $N = 4$. Besides, the configuration of such bending AB and ZB MoSSe/WSSe heterostructure superlattice agrees with the Fourier curve. Our results reveal an effective method to tune the mechanical characteristics of the in-plane Janus TMDs heterostructure by engineering the size and interface type for decent applications.

Conflicts of interest

There are no conflicts to declare.

Acknowledgements

The authors thank the Natural Science Foundation of Jiangsu (no. BK20220407), the financial support of National Natural Science Foundation of China (12102323, 11890674), the Fundamental Research Funds for the Central Universities (sxzy012022024) and the China Postdoctoral Science Foundation (2021M692574).

References

1 A. K. Geim and K. S. Novoselov, The rise of graphene, *Nat. Mater.*, 2007, **6**, 183–191.
2 J. Wang, S. Deng, Z. Liu and Z. Liu, The rare two-dimensional materials with Dirac cones, *Natl. Sci. Rev.*, 2015, **2**, 22–39.
3 T. Roy, M. Tosun, J. S. Kang, A. B. Sachid, S. B. Desai, M. Hettick, C. C. Hu and A. Javey, Field-effect transistors built from all two-dimensional material components, *ACS Nano*, 2014, **8**, 6259–6264.
4 B. Radisavljevic, A. Radenovic, J. Brivio, V. Giacometti and A. Kis, Single-layer MoS_2 transistors, *Nat. Nanotechnol.*, 2011, **6**, 147–150.
5 H. L. Zhuang and R. G. Hennig, Computational search for single-layer transition-metal dichalcogenide photocatalysts, *J. Phys. Chem. C*, 2013, **117**, 20440–20445.
6 Y. Ouyang, C. Ling, Q. Chen, Z. Wang, L. Shi and J. Wang, Activating Inert Basal Planes of MoS_2 for Hydrogen Evolution Reaction through the Formation of Different Intrinsic Defects, *Chem. Mater.*, 2016, **28**, 4390–4396.
7 A. Y. Lu, H. Zhu, J. Xiao, C. P. Chuu, Y. Han, M. H. Chiu, C. C. Cheng, C. W. Yang, K. H. Wei, Y. Yang, Y. Wang, D. Sokaras, D. Nordlund, P. Yang, D. A. Muller, M. Y. Chou, X. Zhang and L. J. Li, Janus monolayers of transition metal dichalcogenides, *Nat. Nanotechnol.*, 2017, **12**, 744–749.
8 H. Qin, K. Ren, G. Zhang, Y. Dai and G. Zhang, Lattice thermal conductivity of Janus MoSSe and WSSe monolayers, *Phys. Chem. Chem. Phys.*, 2022, **24**, 20437.
9 K. Ren, S. Wang, Y. Luo, J.-P. Chou, J. Yu, W. Tang and M. Sun, High-efficiency photocatalyst for water splitting: a Janus MoSSe/XN (X = Ga, Al) van der Waals heterostructure, *J. Phys. D: Appl. Phys.*, 2020, **53**, 185504.
10 R. Peng, Y. Ma, S. Zhang, B. Huang and Y. Dai, Valley Polarization in Janus Single-Layer MoSSe via Magnetic Doping, *J. Phys. Chem. Lett.*, 2018, **9**, 3612–3617.
11 H. Cai, Y. Guo, H. Gao and W. Guo, Tribo-piezoelectricity in Janus transition metal dichalcogenide bilayers: A first-principles study, *Nano Energy*, 2019, **56**, 33–39.
12 C. Shang, X. Lei, B. Hou, M. Wu, B. Xu, G. Liu and C. Ouyang, Theoretical Prediction of Janus MoSSe as a Potential Anode Material for Lithium-Ion Batteries, *J. Phys. Chem. C*, 2018, **122**, 23899–23909.
13 L. Shi, C. Ling, Y. Ouyang and J. Wang, High intrinsic catalytic activity of two-dimensional boron monolayers for the hydrogen evolution reaction, *Nanoscale*, 2017, **9**, 533–537.
14 J. He, S. Li, A. Bandyopadhyay and T. J. N. L. Frauenheim, Unravelling photoinduced interlayer spin transfer dynamics in two-dimensional nonmagnetic-ferromagnetic van der Waals heterostructures, *Nano Lett.*, 2021, **21**, 3237–3244.
15 J. He and T. Frauenheim, Optically driven ultrafast magnetic order transitions in two-dimensional ferrimagnetic MXenes, *J. Phys. Chem. Lett.*, 2020, **11**, 6219–6226.
16 P. Zhang, L. Ma, F. Fan, Z. Zeng, C. Peng, P. E. Loya, Z. Liu, Y. Gong, J. Zhang, X. Zhang, P. M. Ajayan, T. Zhu and J. Lou, Fracture toughness of graphene, *Nat. Commun.*, 2014, **5**, 3782.
17 K. Ren, X. Ma, X. Liu, Y. Xu, W. Huo, W. Li and G. Zhang, Prediction of 2D IV–VI semiconductors: auxetic materials with direct bandgap and strong optical absorption, *Nanoscale*, 2022, **14**, 8463–8473.
18 K. Ren, Y. Yan, Z. Zhang, M. Sun and U. Schwingenschlögl, A family of Li_xB_y monolayers with a wide spectrum of potential applications, *Appl. Surf. Sci.*, 2022, **604**, 154317.
19 B. Wang, Q. Wu, Y. Zhang, L. Ma and J. Wang, Auxetic B_4N Monolayer: A Promising 2D Material with in-Plane Negative Poisson's Ratio and Large Anisotropic Mechanics, *ACS Appl. Mater. Interfaces*, 2019, **11**, 33231–33237.
20 M. Sun and U. Schwingenschlögl, Unique Omnidirectional Negative Poisson's Ratio in δ-Phase Carbon Monochalcogenides, *J. Phys. Chem. C*, 2021, **125**, 4133–4138.
21 R. Lakes, Advances in negative Poisson's ratio materials, *Adv. Mater.*, 1993, **5**, 293–296.
22 Y. Cheng, X. Wu, Z. Zhang, Y. Sun, Y. Zhao, Y. Zhang and G. Zhang, Thermo-mechanical correlation in two-dimensional materials, *Nanoscale*, 2021, **13**, 1425–1442.
23 K. Ren, H. Shu, W. Huo, Z. Cui, J. Yu and Y. Xu, Mechanical, electronic and optical properties of a novel B_2P_6 monolayer: ultrahigh carrier mobility and strong optical absorption, *Phys. Chem. Chem. Phys.*, 2021, **23**, 24915–24921.
24 R. Zhang, L. Zhang, Q. Zheng, P. Gao, J. Zhao and J. Yang, Direct Z-scheme water splitting photocatalyst based on two-

dimensional Van Der Waals heterostructures, *J. Phys. Chem. Lett.*, 2018, **9**, 5419–5424.

25 Y. Gong, J. Lin, X. Wang, G. Shi, S. Lei, Z. Lin, X. Zou, G. Ye, R. Vajtai, B. I. Yakobson, H. Terrones, M. Terrones, B. K. Tay, J. Lou, S. T. Pantelides, Z. Liu, W. Zhou and P. M. Ajayan, Vertical and in-plane heterostructures from WS_2/MoS_2 monolayers, *Nat. Mater.*, 2014, **13**, 1135–1142.

26 H. Qin, Q. X. Pei, Y. Liu and Y. W. Zhang, The mechanical and thermal properties of MoS_2-WSe_2 lateral heterostructures, *Phys. Chem. Chem. Phys.*, 2019, **21**, 15845–15853.

27 D. B. Trivedi, G. Turgut, Y. Qin, M. Y. Sayyad, D. Hajra, M. Howell, L. Liu, S. Yang, N. H. Patoary, H. Li, M. M. Petric, M. Meyer, M. Kremser, M. Barbone, G. Soavi, A. V. Stier, K. Muller, S. Yang, I. S. Esqueda, H. Zhuang, J. J. Finley and S. Tongay, Room-Temperature Synthesis of 2D Janus Crystals and their Heterostructures, *Adv. Mater.*, 2020, **32**, e2006320.

28 K. Ren, H. Qin, H. Liu, Y. Chen, X. Liu and G. Zhang, Manipulating Interfacial Thermal Conduction of 2D Janus Heterostructure via a Thermo-Mechanical Coupling, *Adv. Funct. Mater.*, 2022, **32**, 2110846.

29 C. Jin, E. C. Regan, A. Yan, M. Iqbal Bakti Utama, D. Wang, S. Zhao, Y. Qin, S. Yang, Z. Zheng, S. Shi, K. Watanabe, T. Taniguchi, S. Tongay, A. Zettl and F. Wang, Observation of moire excitons in WSe_2/WS_2 heterostructure superlattices, *Nature*, 2019, **567**, 76–80.

30 Z. Zhang, P. Chen, X. Duan, K. Zang, J. Luo and X. Duan, Robust epitaxial growth of two-dimensional heterostructures, multiheterostructures, and superlattices, *Science*, 2017, **357**, 788–792.

31 L. Ponomarenko, R. Gorbachev, G. Yu, D. Elias, R. Jalil, A. Patel, A. Mishchenko, A. Mayorov, C. Woods and J. Wallbank, Cloning of Dirac fermions in graphene superlattices, *Nature*, 2013, **497**, 594–597.

32 Z. Shi, C. Jin, W. Yang, L. Ju, J. Horng, X. Lu, H. A. Bechtel, M. C. Martin, D. Fu and J. Wu, Gate-dependent pseudospin mixing in graphene/boron nitride moiré superlattices, *Nat. Phys.*, 2014, **10**, 743–747.

33 G. Ding, J. He, G. Y. Gao and K. Yao, Two-dimensional MoS_2-$MoSe_2$ lateral superlattice with minimized lattice thermal conductivity, *J. Appl. Phys.*, 2018, **124**, 165101.

34 F. Wu, T. Lovorn and A. H. MacDonald, Topological exciton bands in moiré heterojunctions, *Phys. Rev. Lett.*, 2017, **118**, 147401.

35 H. Zhang, D. Deng, D. F. Zou, X. B. Li, Z. K. Tang, X. L. Wei, Q. X. Ge and W. J. Yin, The unique photoelectronic properties of the two-dimensional Janus MoSSe/WSSe superlattice: a first-principles study, *Dalton Trans.*, 2022, **51**, 16102–16110.

36 L. Yu, W. Guo, S. Sun and X. Ye, The Strain and Electric Field Effects on the Electronic and Optical Properties of Armchair MoSSe/WSSe Superlattice Nanoribbon: A First-Principles Study, *Phys. Status Solidi B*, 2021, **258**, 2000361.

37 L. Yu, S. Sun and X. Ye, Electronic and magnetic properties of the Janus MoSSe/WSSe superlattice nanoribbon: a first-principles study, *Phys. Chem. Chem. Phys.*, 2020, **22**, 2498–2508.

38 S. Plimpton, Fast parallel algorithms for short-range molecular dynamics, *J. Comput. Phys.*, 1995, **117**, 1–19.

39 A. Stukowski, Visualization and analysis of atomistic simulation data with OVITO–the Open Visualization Tool, *Modell. Simul. Mater. Sci. Eng.*, 2009, **18**, 015012.

40 J.-W. Jiang, Misfit Strain-Induced Buckling for Transition-Metal Dichalcogenide Lateral Heterostructures: A Molecular Dynamics Study, *Acta Mech. Solida Sin.*, 2018, **32**, 17–28.

41 J.-W. Jiang, H. S. Park and T. Rabczuk, Molecular dynamics simulations of single-layer molybdenum disulphide (MoS_2): Stillinger-Weber parametrization, mechanical properties, and thermal conductivity, *J. Appl. Phys.*, 2013, **114**, 064307.

42 R. C. Cooper, C. Lee, C. A. Marianetti, X. Wei, J. Hone and J. W. Kysar, Nonlinear elastic behavior of two-dimensional molybdenum disulfide, *Phys. Rev. B: Condens. Matter Mater. Phys.*, 2013, **87**, 035423.

43 S. Bertolazzi, J. Brivio and A. Kis, Stretching and breaking of ultrathin MoS_2, *ACS Nano*, 2011, **5**, 9703–9709.

44 C. Zhang, M. Y. Li, J. Tersoff, Y. Han, Y. Su, L. J. Li, D. A. Muller and C. K. Shih, Strain distributions and their influence on electronic structures of WSe_2-MoS_2 laterally strained heterojunctions, *Nat. Nanotechnol.*, 2018, **13**, 152–158.

45 J. Zhou, J. Lin, X. Huang, Y. Zhou, Y. Chen, J. Xia, H. Wang, Y. Xie, H. Yu, J. Lei, D. Wu, F. Liu, Q. Fu, Q. Zeng, C. H. Hsu, C. Yang, L. Lu, T. Yu, Z. Shen, H. Lin, B. I. Yakobson, Q. Liu, K. Suenaga, G. Liu and Z. Liu, A library of atomically thin metal chalcogenides, *Nature*, 2018, **556**, 355–359.

46 C. Huang, S. Wu, A. M. Sanchez, J. J. Peters, R. Beanland, J. S. Ross, P. Rivera, W. Yao, D. H. Cobden and X. Xu, Lateral heterojunctions within monolayer $MoSe_2$-WSe_2 semiconductors, *Nat. Mater.*, 2014, **13**, 1096–1101.

47 T. Ma, W. Ren, X. Zhang, Z. Liu, Y. Gao, L.-C. Yin, X.-L. Ma, F. Ding and H.-M. Cheng, Edge-controlled growth and kinetics of single-crystal graphene domains by chemical vapor deposition, *Proc. Natl. Acad. Sci. U. S. A.*, 2013, **110**, 20386–20391.

48 H. Li, A. W. Contryman, X. Qian, S. M. Ardakani, Y. Gong, X. Wang, J. M. Weisse, C. H. Lee, J. Zhao, P. M. Ajayan, J. Li, H. C. Manoharan and X. Zheng, Optoelectronic crystal of artificial atoms in strain-textured molybdenum disulphide, *Nat. Commun.*, 2015, **6**, 7381.

49 Q. Song, M. An, X. Chen, Z. Peng, J. Zang and N. Yang, Adjustable thermal resistor by reversibly folding a graphene sheet, *Nanoscale*, 2016, **8**, 14943–14949.

50 N. Yang, X. Ni, J.-W. Jiang and B. Li, How does folding modulate thermal conductivity of graphene?, *Appl. Phys. Lett.*, 2012, **100**, 093107.